Supporting Information

Organelle-specific targeting of polymersomes into the cell nucleus

Christina Zelmer[1,2*], Ludovit P. Zweifel[1*], Larisa E. Kapinos[1], Ioana Craciun[2], Zekiye P. Güven[3], Cornelia G. Palivan[2] and Roderick Y.H. Lim[1]

[1]Biozentrum and the Swiss Nanoscience Institute, University of Basel, Klingelbergstrasse 70, CH-4056 Basel, Switzerland

[2]Department of Chemistry, University of Basel, Mattenstrasse 24a, CH-4002 Basel, Switzerland

[3]Institute of Materials, Ecole Polytechnique Fédérale de Lausanne, CH-1015 Lausanne, Switzerland

www.pnas.org/cgi/doi/10.1073/pnas.1916395117

1. Synthesis

1.1 Amphiphilic triblock copolymer $PMOXA_4$-$PDMS_{44}$-$PMOXA_4$

$PMOXA_4$-$PDMS_{44}$-$PMOXA_4$ was synthesized as published (1, 2) with slight modifications. Bifunctional carbinol-terminated poly(dimethylsiloxane) (PDMS) was dissolved in hexane, cooled down to -10°C and reacted with triflic acid anhydride. Triethylamine (TEA) was added to the mixture to neutralize the triflic acid reaction by-product. The precipitated organic salt was removed by filtration through an ice-cooled G4 filter funnel. Afterwards, the filtrate was removed *in vacuo* and a mixture of anhydrous acetonitrile/dichloromethane (1:1, v/v) was added to dissolve the bitriflate-activated PDMS for subsequent reaction steps. Freshly distilled 2-methyl-2-oxazoline (MOXA) was immediately added to initiate polymerization with PDMS at both ends. The reaction was stirred for 60 hours at r.t. and quenched with a TEA/water mixture (1:4, v/v). The resulting polymer mixture was purified by ultrafiltration using a water/EtOH mixture (1:2, v/v) and extracted with a MeOH/hexane solvent combination (1:1, v/v). The final product was characterized by ^{1}H NMR and GPC giving a final composition of $PMOXA_4$-$PDMS_{44}$-$PMOXA_4$ (M_n = 4000 Da, molar-mass dispersity, $Đ_M$ = 1.7) with a hydrophilic-to-total molecular mass ratio *f* of 29 %.

Isolated yield: 28 %; ^{1}H NMR (400 MHz, $CDCl_3$) d/ppm: 3.97 – 3.31 (bm, 8H, CH_2NCH_2), 2.32 – 2.07 (bs, 6H, $C(O)CH_3$), 1.65 – 1.53 (bm, 4H, $CH_2CH_2CH_2$), 0.56 – 0.45 (bm, 4H, $SiCH_2$), 0.28 – (- 0.13) (bs, 6H, $SiCH_3$)

1.2 Furan protected maleimide linker (FMal-linker)

FMal-linker synthesis followed procedures described previously (3, 4). Specifically, a furan-maleic anhydride Diels-Alder adduct (DA adduct 3a,4,7,7a-tetrahydro-4,7-epoxysobenzofuran-1,3-dione; 4.5 g, 27.1 mmol) and Na_2CO_3 (2.87 g, 27.1 mmol) were dissolved in 100 ml MeOH and a solution of *b*-alanine (2.41 g, 27.1 mmol) in 100 ml MeOH was thereupon added. The reaction mixture was stirred for 6 days at 56 °C until the solvent was removed and the resulting white residue was then re-dissolved in 100 ml CH_2Cl_2. The solution was extracted 4 times with 80 ml of 0.6 M aqueous HCl and the collected organic phase dried over anhydrous $MgSO_4$ and filtered. Removal of CH_2Cl_2 under reduced pressure yielded the FMal-linker as white crystalline powder after which the structure was identified *via* ^{1}H NMR.

Isolated yield: 52 %; ^{1}H NMR (400 MHz, $CDCl_3$) d/ppm: 6.51 (t, 2H, CH=CH), 5.27 (t, 2H, CHOCH), 3.79 (t, 2H, $NCH_2CH_2(O)O$), 2.87 (d, 2H, CHC(O)N), 2.68 (t, 2H, CH_2COOH)

1.3 Maleimide linker end-group functionalized $PMOXA_4$-$PDMS_{34}$-$PMOXA_4$

Previous procedures (5, 6) were adopted for the end-group functionalization of $PMOXA_4$-$PDMS_{44}$-$PMOXA_4$ with maleimide linking groups. First, FMal (23 mg, 97.2 mmol) was dissolved in 3 ml anhydrous CH_2Cl_2 under rigorous stirring and subsequently 4-(dimethylamino)-pyridin (DMAP) (11.9 mg, 97.2 mmol) and $PMOXA_4$-$PDMS_{44}$-$PMOXA_4$ (100 mg, 24.3 mmol) were added. The reaction mixture was cooled down to 0 °C, and then *N*,*N*′-dicyclohexylcarbodiimid (DCC) (20 mg, 97.2 mmol) was added under stirring for 5 minutes. Thereafter, cooling was stopped and the solution continuously stirred for 10 hours. The resulting precipitated by-product dicyclohexylurea (DCU) was filtered off and the solvent removed from the filtrate *in vacuo*. The remaining

residue was dissolved in EtOH and then purified using dialysis tubing with molecular mass cut-off 3.5 kDa, once for 2 hours against EtOH/H_2O (1:1, v/v) and twice against deionized water for 2 hours each. Importantly, the ^{1}H NMR spectrum recorded for the lyophilized FMal-linker end-group functionalized PMOXA$_4$-PDMS$_{44}$-PMOXA$_4$ featured all product specific peaks including the ester connective methylene protons at 2.64 ppm shift and the furan protons at 2.85 ppm (h), 5.25 ppm (j) and 6.50 ppm (k) (**Fig. S1**). It further revealed a PMOXA$_4$-PDMS$_{44}$-PMOXA$_4$ conjugation efficacy with FMal of > 73 % that however still contained traces of residual DCU.

Isolated yield: 65 %; ^{1}H NMR (400 MHz, $CDCl_3$) d/ppm: 6.54 - 6.47 (bm, 4H, CH=CH), 5.29 – 5.20 (bm, 4H, CHOCH), 3.86 – 3.71 (bm, 4H, $NCH_2CH_2(O)O$), 3.66 – 3.32 (bm, 8H, CH_2NCH_2), 2.89 – 2.80 (bm, 4H, CH(O)N), 2.72 – 2.56 (bm, 4H, $CH_2(O)O$), 2.25 – 2.02 (bs, 6H, $C(O)CH_3$), 1.67 – 1.56 (bm, 4H, $CH_2CH_2CH_2$), 0.55 – 0.46 (bm, 4H, $SiCH_2$), 0.33 – (- 0.27) (bs, 6H, $SiCH_3$)

Next, the furan protected polymer intermediate was dissolved in 10 ml toluene and heated up to 100 °C under continuous stirring. The thermally induced retro Diels-Alder furan deprotection was monitored by ^{1}H NMR to determine the reaction end point and was stopped after 9 hours of refluxing. As the reaction evolved, the furan proton peaks (at 2.85 ppm (h), 5.25 ppm (j) and 6.50 ppm (k) in **Fig. S1**) disappeared almost entirely whilst the olefinic maleimide proton peak simultaneously arose at 6.70 ppm shift (h'). The ^{1}H NMR spectrum recorded for the final lyophilized product revealed a triblock copolymer composition of Mal-PMOXA$_4$-PDMS$_{34}$-PMOXA$_4$-Mal with 34% of all polymer end-groups being substituted with active maleimide linking sites. The additional purification step most likely caused the reduction in PDMS units due to higher molecular

weight polymer chains being less soluble in toluene. The resulting polymer was obtained at 95 % isolated yield being fully conjugated on both end-sides with maleimide linker. This yielded an average molecular mass of M_n = 3800 Da (^{1}H NMR) and a hydrophilic-to-total molecular mass ratio *f* of 32%. GPC analysis in DMF yielded a molecular weight dispersity, $Đ_M$ of 2.8.

Isolated yield: 95 %; ^{1}H NMR (400 MHz, $CDCl_3$) d/ppm: 6.74 - 6.67 (bm, 4H, CH=CH), 3.87 – 3.75 (bm, 4H, $NCH_2CH_2(O)O$), 3.64 – 3.28 (bm, 8H, CH_2NCH_2), 2.79 – 2.59 (bm, 4H, $CH_2C(O)O$), 2.25 – 2.02 (bs, 6H, $C(O)CH_3$), 1.65 – 1.59 (bm, 4H, $CH_2CH_2CH_2$), 0.56 – 0.46 (bm, 4H, $SiCH_2$), 0.27 – (- 0.13) (bs, 6H, $SiCH_3$)

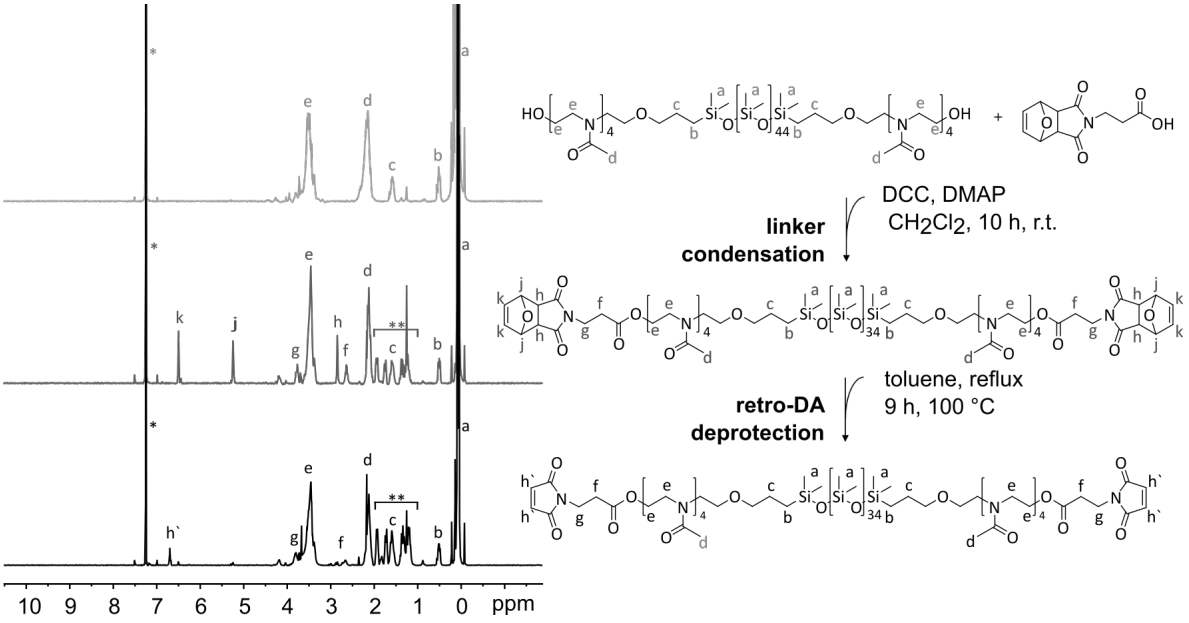

Figure S1. Polymer synthesis. The two-step synthesis of Mal-$PMOXA_4$-$PDMS_{34}$$PMOXA_4$-Mal is monitored by ^{1}H NMR in $CHCl_3$ (*): Condensation of $PMOXA_4$-$PDMS_{44}$-$PMOXA_4$ (top ^{1}H NMR spectrum) with the FMal DA adduct resulting in a polymer intermediate with > 73 % FMal conjugation (intermediate ^{1}H NMR spectrum). Upon thermal furan deprotection, the Mal-$PMOXA_4$-$PDMS_{34}$$PMOXA_4$-Mal conjugate (bottom ^{1}H NMR spectrum) is obtained with > 34 % of active conjugated maleimide linking sites.

2. Polymersome preparation

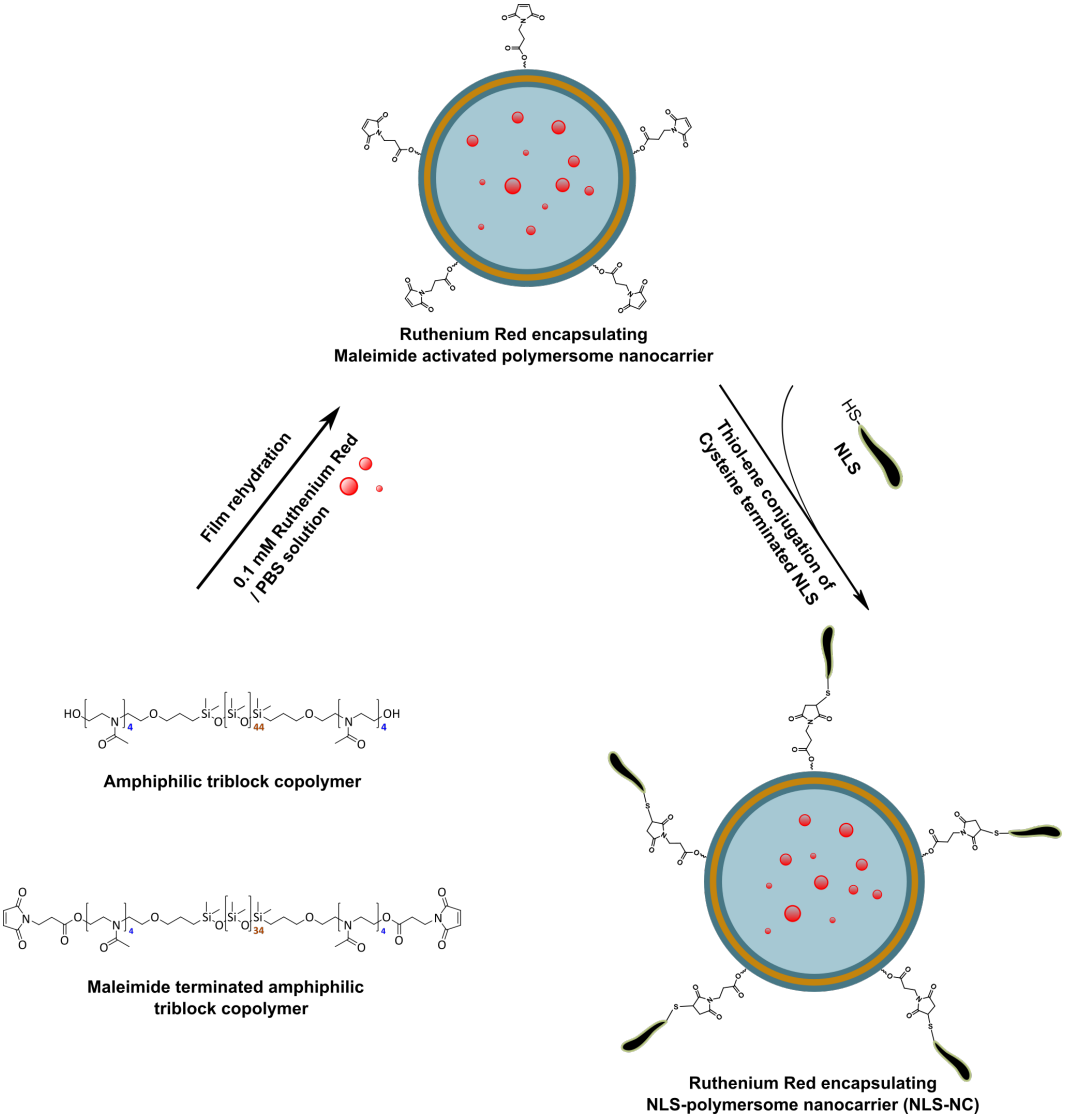

Figure S2. Preparation of NLS-NCs. $PMOXA_4$-$PDMS_{44}$-$PMOXA_4$ and Mal-$PMOXA_4$-$PDMS_{34}$-$PMOXA_4$-Mal spontaneously self-assemble into Mal-NCs that encapsulate RR. Cysteine modified NLS are conjugated to the Mal-NLS membrane *via* a spontaneous thiol-ene coupling reaction. See Methods in main text for details.

3. Polymersome characterization

3.1 Molecular composition and supramolecular architecture *via* SLS and DLS

Polymersome size, morphology, shape and aggregation number were assessed by static (SLS) and dynamic light scattering (DLS) using a commercial goniometer (LS instruments) equipped with a 30 mW HeNe laser (wavelength 633 nm) and two parallel avalanche photomultiplier detectors (APDs). The detected count rate was set to 40 kHz *via* an automatic laser intensity regulation function. APD afterpulsing effects were antagonized by pseudo cross-correlation between the signals detected in the two APDs. NC scattering intensity was measured in dust-free 10 mm high precision quartz cells placed in a thermostat vat at 298 K.

Careful evaluation of SLS data is required since optical variations between the loaded-NC interior and surrounding media may lead to additional scattering vector contributions. Accordingly, we compared the scattering patterns of RR-encapsulating blank NCs (75 mM RR in PBS) against empty blank NCs (only PBS). Average scattering intensities were examined for different NC concentrations (0.15, 0.3, 0.4 and 0.5 mg/ml dilutions in PBS) and scattering angles (from 40° to 110°, with a step width of 10° and a signal integration time of 20 s per step). The averaged results of three independent measurements are summarized in Berry plots (**Fig. S3A and B**). By extrapolating to zero concentration ($c \rightarrow 0$) and zero scattering angle ($\theta \rightarrow 0$), we extracted NC radius of gyration R_g, average supramolecular mass M_w and the second virial coefficient A_2. NC hydrodynamic radii R_h distributions were further validated by DLS performed at 90° scattering angle on 0.15 mg/ml diluted polymersome solution

over a signal integration time of 60 s (**Fig. S3C**). A summary of both SLS and DLS measurements is found in Table S1.

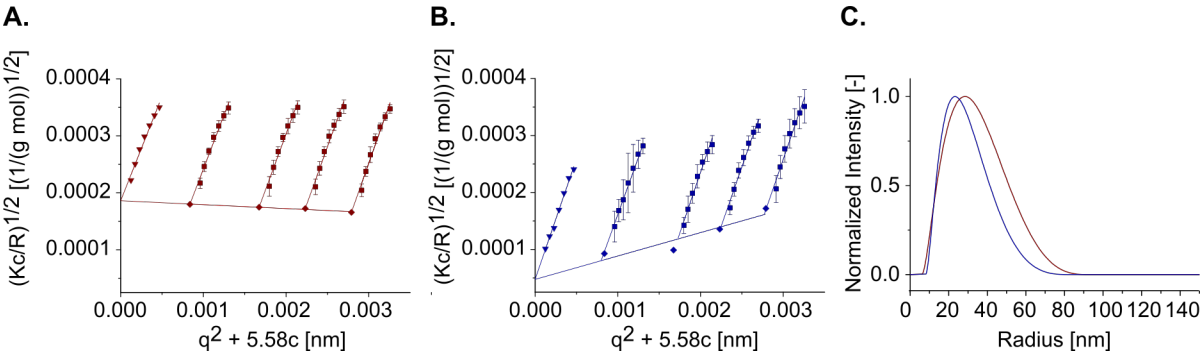

Figure S3. Characterization by static and dynamic light scattering. Berry plots constructed from the concentration and angular dependent scattering intensities of **A.** blank RR-encapsulating NCs and **B.** blank PBS-encapsulating NCs. *R* is the so-called Rayleigh excess ratio that corrects for the scattering signal contribution of the pure solvent, *K* is an optical constant factor and *q* is an angular dependent scattering vector. **C.** Radii distributions of RR- (red) and PBS-encapsulating (blue) NCs as determined by DLS.

To evaluate NC morphology, we calculated the form factor, $r = R_g/R_h$, which approaches unity if the assemblies are hollow vesicles (7). From **Table S1**, both RR- (r = 0.88) and PBS-encapsulating blank NCs (r = 1.09) give r values close to unity. In terms of NC mass (M_{NC}), we obtain 88.3 ± 2.1 MDa and 71.5 ± 15.9 MDa for the RR- and PBS-encapsulating blank NCs, respectively, which indicates that RR encapsulation did not influence the polymersome architecture nor their size. By this analysis, each 2 mg/ml stock solution is estimated to contain 23 nM and 28 nM of RR- and PBS-encapsulating blank NCs, respectively.

Table S1: SLS/DLS characterization of blank NCs encapsulating either 75 mM RR in PBS or only PBS.

LS results	dn/dc* [ml g^{-1}]	M_{NC} [10^6 g mol^{-1}]	A_2 [mol ml g^{-2}]	R_g [nm]	R_h [nm]	P** [-]	r [-]
RR encapsulating blank NCs	0.188	88.3 ± 2.1	(9.76 ± 1.23) E-8	25.3 ± 0.3	28.6 ± 14.0	22100	0.88
PBS encapsulating blank NCs	0.188	71.5 ± 15.9	(3.68 ± 1.40) E-7	26.5 ± 3.0	24.3 ± 10.4	17900	1.09

*Indices taken from literature (1)
**Aggregation number p with M_n = 4000 Da of $PMOXA_4$-$PDMS_{44}$-$PMOXA_4$

To ascertain M_W, R_g and r for NLS-NCs, we used dn/dc = 0.188 as determined previously for PMOX-PDMS-PMOXA polymersomes (1). Accordingly, a 2 mg/ml RR-NLS-NC stock solution was equivalent to 23 nM.

3.2 Surface conjugation to Mal-NCs *via* fluorescence correlation spectroscopy (FCS)

A fluorescence correlation spectroscopy (FCS)-based binding assay was used to evaluate the functionality of maleimide-linker end groups being exposed at the surface of Mal-NCs. As NLS itself is not fluorescent, green SAMSA fluorescein (ThermoFischer) was used as a surrogate. Acetyl protected SAMSA was base activated to its thiol-containing form (ThermoFischer protocol) and applied at a 3:2 molar stoichiometry (SAMSA:Mal) to pre-formed Mal-NCs. The catalyst free thiol-ene `click` reaction was allowed to proceed overnight whereupon the resulting SAMSA-Mal-NC conjugates (hereafter SAMSA-NCs) were purified from unreacted SAMSA *via* size exclusion chromatography through a Sephadex G-25 column.

Next, the number of Mal-NC-bound SAMSA probes was measured by FCS, using a Zeiss LSM 510-META/Confcor2 laser-scanning microscope, equipped with an Argon2-laser (488 nm) and operated at 17 mW laser power. A 40x water-immersion objective (Zeiss C/Apochromat 40X, NA 1.2) and appropriate BP 505 – 550 nm filters were used and the pinhole adjusted to 70 µm with 5% excitation transmission. The confocal volume - an ellipsoid with a xy-axis radius ω_0 and a z-axis radius ω_z - was calibrated with Oregon Green 488 of known diffusion constants D of 411 mm^2/s at 298 K (8). Thirty 10 s long intensity fluctuation time traces were time correlated for a 0.24 nM SAMSA-NC dilution in PBS and separately for 2 nM free SAMSA in PBS. The resulting auto-correlation curves $G(\tau)$ were fitted to a multi-component model of three-dimensional diffusion containing one triplet term and a diffusional term

$$G(\tau) = G^0 \cdot \underbrace{\left[\frac{(1-T+Te^{-\frac{\tau}{\tau_T}})}{(1-T)}\right]}_{G(\tau)_{triplet}} \cdot \underbrace{\sum_{i=1}^{n} f_i \frac{1}{1+(\frac{\tau}{\tau_{D,i}})} \sqrt{\frac{1}{1+(\frac{\tau}{\tau_{D,i}})(\frac{w_0}{w_z})^2}}}_{G(\tau)_{diffusion}} \quad \text{(S3.1)}$$

with G^0 the initial correlation amplitude for $\tau = 0$, τ_T the characteristic triplet relaxation time and T the fractional triplet contribution, $\tau_{D,i}$ the translational correlation time and f_i the fractional amplitude of the i-th component (**Fig. S4**). Free SAMSA was best described by a one-component model (n = 1), while SAMSA-NCs contained a second component from free SAMSA that remained in solution even after NC purification (n = 2). Assuming Brownian motion, the diffusion constants of the individual components can be calculated via $D_i = 4\tau_{D,i}\omega_0^2$ and consequently the individual hydrodynamic radii $R_{h,i}$ via the Stokes-Einstein relation.

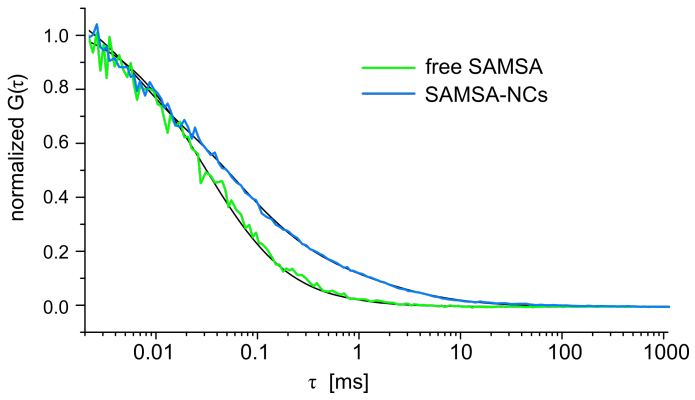

Figure S4. FCS measurements and auto-correlation fits for free SAMSA and SAMSA-NC conjugates. Normalized auto-correlation functions of free SAMSA fluorescein (green) and of SAMSA-NC conjugates (blue).

Subsequently, the number of SAMSA probes per SAMSA-NC was determined by dividing the average brightness of one SAMSA-NC by the average brightness of a single SAMSA molecule, *i.e.* their detected counts per molecule (CPM). The corresponding CPMs were calculated to 37.5 ± 12.5 kHz and 1.4 ± 0.3 kHz, respectively, with the latter being consistent with the CPM obtained when only free SAMSA probes were present in solution (**Table S2**). However, considering that maleimide endgroups may hydrolyse over time and/or SAMSA-NC conjugation may reduce the CPM yields a lower limit of 27 ± 9 SAMSA entities linked to a single 50 nm-diameter Mal-NC with a grafting distance of 8.5 ± 1.1 nm.

Table S2: FCS measurements and auto-correlation fits for free SAMSA and SAMSA-NC conjugates

	D [μm^2/s]	f_i [-]	R_h [nm]	CPM [kHz]
free SAMSA (1-component)	291.4 ± 39.5	1	0.8 ± 0.1	1.4 ± 0.3
SAMSA-NCs (2-components)	7.4 ± 2.5	0.84	33.1 ± 8.4	37.5 ± 12.5
	271.5 ± 227.0	0.16	0.9 ± 0.4	1.4 ± 0.3

4. Dual colour fluorescence lifetime cross-correlation spectroscopy (dcFLCCS)

Time-gated dcFLCCS measurements were conducted with a confocal volume overlap of 92 % and lifetime corrected in a step-wise manner (see main text):

I. Fluorescence intensity fluctuation time traces $F_{uncorrected}(t)$ were recorded in two channels (530 nm and 640 nm), and the initial uncorrected autocorrelation (AC) and cross-correlation (CC) curves constructed.

II. Parallel to $F_{uncorrected}(t)$, time correlated single photon counting (TCSPC) was used to generate photon arrival time histograms and the resulting fluorescence intensity decays *I(t)* were fitted to multi-exponentials

$$I(t) = I_b + \sum_{i=0}^{n-1} \alpha_i exp\left(-\frac{t-t_0}{\tau_{L,i}}\right) \quad \text{(S4.1)}$$

with α_i the amplitude and $\tau_{L,i}$ the fluorescence lifetime of the *i*-th component, I_b the non-decaying background intensity and t_0 the zero-time shift.

III. Lifetime decays from **II**. were used to weigh the contribution of each photon in order to correct the AC and CC curves from **I**.

All data was processed and analysed with SymphoTime64 (PicoQuant).

5. dcFLCCS analysis of cargo encapsulation

Dye specific fluorescent decays of NLS-NCs containing either RR or Bodipy were obtained in order to perform a lifetime correction on each individual channel (**Fig. S5**). Lifetime-corrected ACs were fit to a one- (Bodipy) or two-component (RR) model for three-dimensional diffusion (**Eq. S3.1**) and diffusion constants and hydrodynamic radii calculated according to **Supporting Information 3.2**. Both RR and Bodipy exhibit

decays that show pronounced shifts towards longer lifetime values (**Fig. S5A and B**), indicating that their fluorescent lifetimes τ_L are sensitive to the NLS-NC chemical environment. From fluorescence lifetime correlation spectroscopy (FLCS), RR-NLS-NCs give D = 7.6 ± 3.3 μm^2/s (R_h = 31.9 ± 18.4 nm) as compared to free RR D = 455 ± 21 μm^2/s (R_h = 0.5 ± 0.0 nm; **Fig. 2d inset**). Likewise, Bodipy-NLS-NCs give D = 9.06 ± 0.11 μm^2/s (R_h = 23.0 ± 1.3 nm) in comparison to free Bodipy with D = 359 ± 25 μm^2/s (R_h = 0.81 ± 0.06 nm; **Fig. S5C**). Thus, both the lifetime decays and the measured FLCS curves demonstrate the successful incorporation of RR and Bodipy into NLS-NCs, respectively. With this analysis in hand, dcFLCCS was used to verify the co-existence of RR in the aqueous lumen and Bodipy in the amphiphilic membrane of NLS-NCs, respectively. This was analysed using 0.02 mg/ml ($M_{NLS\text{-}NC}$≈ 88 MDa; n = 0.24 nM) NLS-NC samples by cross-correlating RR and Bodipy, which emit in the red and the far red, respectively (**see main text and Fig. 2**).

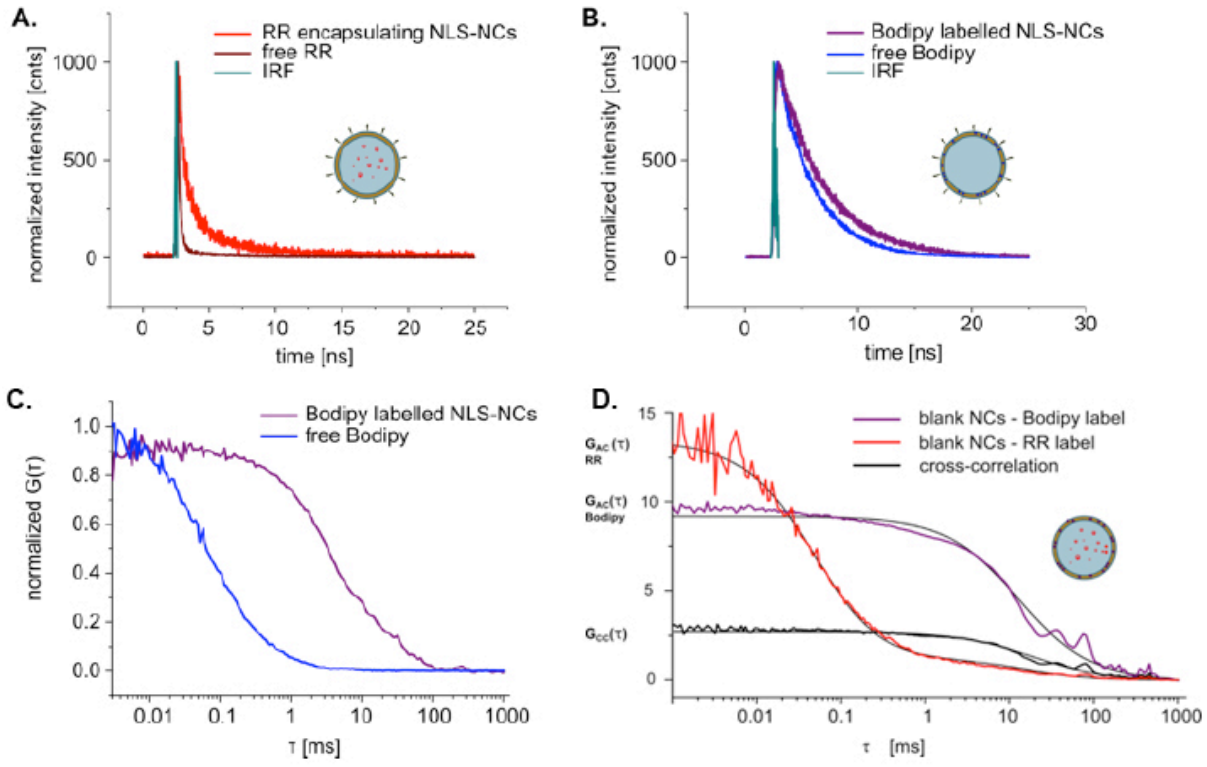

Figure S5. Normalized fluorescence lifetime spectra recorded for **(A)** RR encapsulated NLS-NCs in the 530 nm red channel, and **(B)** Bodipy labelled NLS-NCs in the 640 nm far red channel. Each plot includes the respective free RR or Bodipy lifetime spectra that shift towards longer exponential decay times, indicating successful NLS-NC encapsulation. Instrument response functions (IRF) of the measurement system are included (green). (**C**) Bodipy intercalation into the NLS-NC membrane results in a pronounced shift of the auto-correlation curve towards longer diffusion times in comparison to free Bodipy. (**D**) Blank NCs co-encapsulate RR within their lumen and incorporate Bodipy inside their membranes. dcFLCCS identifies their co-localization based on the high cross-correlation amplitude.

For blank NCs, we obtained diffusion coefficients of D = 7.6 ± 0.2 μm^2/s and D = 5.6 ± 0.1 μm^2/s from the RR and Bodipy signals, which correspond to comparable hydrodynamic radii of R_h = 30.4 ± 0.8 nm and R_h = 41.3 ± 0.8 nm, respectively. In addition, the large cross-correlation amplitude $G_{CC}(0)$ (**Fig. S5D**) arises from the

fractional co-localization of RR and Bodipy that integrate together in 30 % of the prepared blank NCs.

6. dcFLCCS analysis of Kapα•Kapβ1 binding to NLS-NCs

dcFLCCS was used to study the binding of Kapα•Kapβ1 (9) to NLS-NC at the single molecule level. To ensure a complete complexation of Kapβ1, we mixed 20 nM Kapβ1 (i.e., comprising of 2 nM Kapβ1-Atto550 and 18 nM unlabelled Kapβ1) in PBS with a ten-fold higher concentration of Kapα (i.e., 200 nM). In parallel, 5.7 nM NLS-NCs (M_{NLS-NC}≈ 88 MDa) were freshly labelled with 200 nM Bodipy and purified *via* size exclusion chromatography in PBS. Bodipy-NLS-NCs were titrated from 25 pM to 590 pM in 20 nM Kapα•Kapβ1 with a 30 min incubation time per titration step. By cross correlating the detected Atto550 and Bodipy signals, we could measure (i) the number of Kapα•Kapβ1-bound heterodimers per NLS-NC, and (ii) the upper limit of the dissociation constant of Kapα•Kapβ1 to the NLS. Lifetime corrected AC and CC curves (**Supporting Information S4**), with a maximum correlation integration time of 2 s, were constructed from 120 s long intensity time traces and analysed via **equation S3.1** (i.e., AC Bodipy labelled NLS-NCs with n=1; AC Kapα•Kapβ1-Atto-550 with n=2; CC of NLS-NC bound Kapα•Kapβ1 with n=1).

We calculated the relative cross-correlation amplitude (RCA) (10) for each titration step in order to obtain a ligand-receptor binding curve from dcFLCCS measurements. Here, the RCA is a measure of the fraction of Kapα•Kapβ1 bound to NLS-NCs calculated from the initial amplitudes of the CC curve G_{CC}^{0} and of the NLS-NC AC curve G_{NLS-NC}^{0} as follows:

$$RCA = \frac{G^0_{CC}}{G^0_{NLS-NC}} = \frac{[\text{Kap}\alpha/\beta1\bullet\text{NLS}-\text{NC}]}{k \cdot C_{NLS-NC}} \quad \text{(S6.1)}$$

Plotting the bound fraction against the titrated concentration of NLS-NCs (C_{NLS-NC}) yields the desired binding curve (**black squares, Fig. 3B**). The initial Kapα•Kapβ1 concentration $C^0_{Kap\alpha/\beta1}$ was determined *via* UV/VIS spectroscopy (Nanodrop). Because the NLSs on the NLS-NC behave as multiple independent (non-cooperative) binding sites (each binding a single Kapα•Kapβ1 complex) and by introducing correction parameters for titration errors etc. (T_E) and an upper limit for competent Kapα•Kapβ1 (U_L), the binding curve can be fit with (11)

$$T_E + U_L \cdot \frac{k \cdot C_{NLS-NC} + C^0_{Kap\alpha/\beta1} + K_d - \sqrt{\left(k \cdot C_{NLS-NC} + C^0_{Kap\alpha/\beta1} + K_d\right)^2 - 4 \cdot k \cdot C_{NLS-NC} \cdot C^0_{Kap\alpha/\beta1}}}{2 \cdot C^0_{Kap\alpha/\beta1}} \quad \text{(S6.2)}$$

where k is the number of bound Kapα•Kapβ1 complexes per NLS-NC. The abrupt saturation of the binding curve (**Fig. 3B**) suggests tight binding. Therefore, we first fixed the K_D of the Kapα•Kapβ1•NLS-NC interaction to 10^{-15} M and obtained k = 57 ± 3, T_E = -0.06 and U_L = 0.76 with an R^2 = 0.984. In a next step, we fixed k = 57 and performed an *F*-test analysis to find that the upper limit of the 95% confidence interval on K_D = 0.4 nM (**black line, Fig. 3B**).

Next, we used the fit parameters (k, K_D, T_E and U_L) to describe the dependence of freely diffusing Kapα•Kapβ1 complexes $C^{free}_{Kap\alpha/\beta1}$ on the NLS concentration

$$C_{NLS} = C_{NLS-NC} \cdot k \quad \text{(S6.3)}$$

At equilibrium, the total Kapα•Kapβ1 concentration equals the sum of free and NLS-NC bound Kapα•Kapβ1:

$$C^0_{Kap\alpha/\beta1} = C^{free}_{Kap\alpha/\beta1} + C_{NLS-NC} \cdot k = C^{free}_{Kap\alpha/\beta1} + C_{NLS} \quad \text{(S6.4)}$$

The calibration of the effective confocal volumes V_{eff} *via* bead scans (**Supporting Information S4**) allows to calculate the concentration of freely diffusing Kapα•Kapβ1 complexes $C^{free}_{Kap\alpha/\beta1}$ from the total Kapα•Kapβ1 concentration $C^0_{Kap\alpha/\beta1}$ based on the RCA (12):

$$\frac{G^0_{CC}}{G^0_{NLS-NC}} = \frac{V_{eff,NLS-NC}}{V_{eff,CC}} \frac{C^0_{Kap\alpha/\beta1} - C^{free}_{Kap\alpha/\beta1}}{C^0_{Kap\alpha/\beta1}} \quad \text{(S6.5)}$$

Finally, by considering equations S6.2, S6.3 and S6.4, we can write

$$C^{free}_{Kap\alpha/\beta1} = \frac{V_{eff,CC}}{V_{eff,NLS-NC}} \cdot (1 - T_E) \cdot \left(C^0_{Kap\alpha/\beta1} - U_L \cdot \frac{C_{NLS} + C^0_{Kap\alpha/\beta1} + K_d - \sqrt{\left(C_{NLS} + C^0_{Kap\alpha/\beta1} + K_d\right)^2 - 4 \cdot C_{NLS} \cdot C^0_{Kap\alpha/\beta1}}}{2} \right) \quad \text{(S6.6)}$$

The dependence of the free Kapα•Kapβ1 concentration $C^{free}_{Kap\alpha/\beta1}$ on the titrated concentration of NLS C_{NLS} (**blue circles, Fig. 3B**) can then be simulated by equation S6.6 (blue line in Fig. 3b) using the obtained parameters $V_{eff,CC}$, $V_{eff,NLS-NC}$, K_D, T_E and U_L.

The effect of the lifetime correction on eliminating artefacts such as false-positive cross-correlation due to parasitic signals (i.e. spectral cross-talk) is shown in **Fig. S6**. While lifetime correction did not alter the CC amongst NLS-NCs and Kapα•Kapβ1 (**Fig. S6A**), cross-correlation between blank NCs and Kapα•Kapβ1 was identified as an artefact (**Fig. S6B**). This indicates that Kapα•Kapβ1 specifically binds NLS rather than

interacting non-specifically with the $PMOXA_4$-$PDMS_{44}$-$PMOXA_4$ membrane. Likewise, standalone Atto550 does not interact with the NLS-NCs, proving that the NLS-NC binding with Kapα•Kapβ1 is mediated by Kaps and not by its label Atto-550 (**Fig. S6C**).

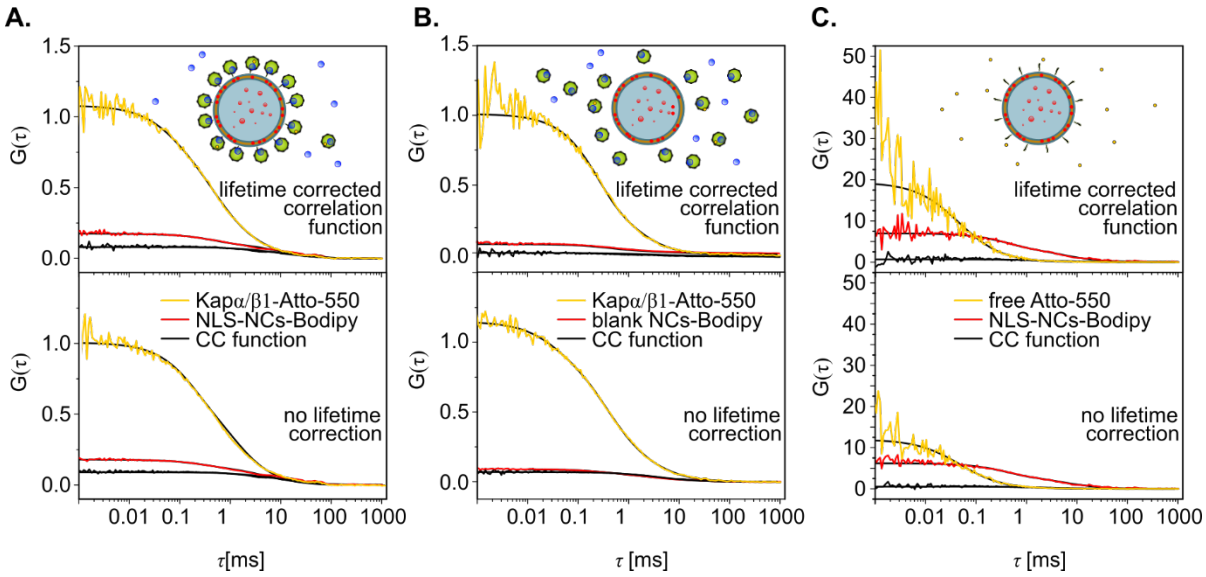

Figure S6. *ACs* and *CCs* are displayed before and after lifetime correction for **(A)** Kapα•Kapβ1-Atto550 with Bodipy stained NLS-NCs, **(B)** Kapα•Kapβ1-Atto550 with Bodipy stained blank NCs and **(C)** free Atto550 mixed with Bodipy stained NLS-NCs.

7. SPR analysis of Kapα•Kapβ1•NLS-NCs binding to FG nucleoporins

Surface Plasmon Resonance (SPR) spectroscopy was used to study FG Nup-binding of Kapα•Kapβ1•NLS-NCs. This was performed at 298 K on a BiacoreT200 (GE Healthcare) equipped with a flow cell with four parallel flow channels. As detailed previously (13, 14), SPR sensograms were obtained using a gold sensor chip with two flow channels conjugated with cysteine-terminated FG Nups (i.e., Nup98, Nup214, or Nup153) and two flow channels conjugated with $HS\text{-}(CH_2)_{11}\text{-}(OCH_2\text{-}CH_2)_3\text{-}OH$ (Nanoscience) as a non-specific reference. A 1% BSA (Sigma Aldrich) and 1 mM $MgCl_2$ containing PBS (Gibco by Life Technologies, pH 7.2) running buffer was used. Ten

titrations (increasing by factor 2) of Kapα:Kapβ1 (at a ratio of 10:1) to a maximum concentration of 100 nM Kapβ1 and 1000 nM Kapα were used. The ratio of NLS-NCs/blank NCs to Kapα•Kapβ1 was kept constant by mixing each Kapα•Kapβ1 solution with a factor 2 increase of NLS-NCs/blank NCs terminating with a final mass concentration of 100 mg/ml of NLS-NCs/blank NCs (for 100 nM Kapβ1 and 1000 nM Kapα). The NCs were incubated with Kap complexes for 12 h before being injected at a flow rate of 10 µl/min. Representative sensograms used in Langmuir isotherm analyses (**Fig. 4**) are shown in **Fig. S7A to C.** Separately, we showed that neither blank NCs nor NLS-NCs interacted with the FG Nups in the absence of Kapα•Kapβ1 (**Fig. S7D**). The respective equilibrium dissociation constants (K_D) are summarized in **Table S3**.

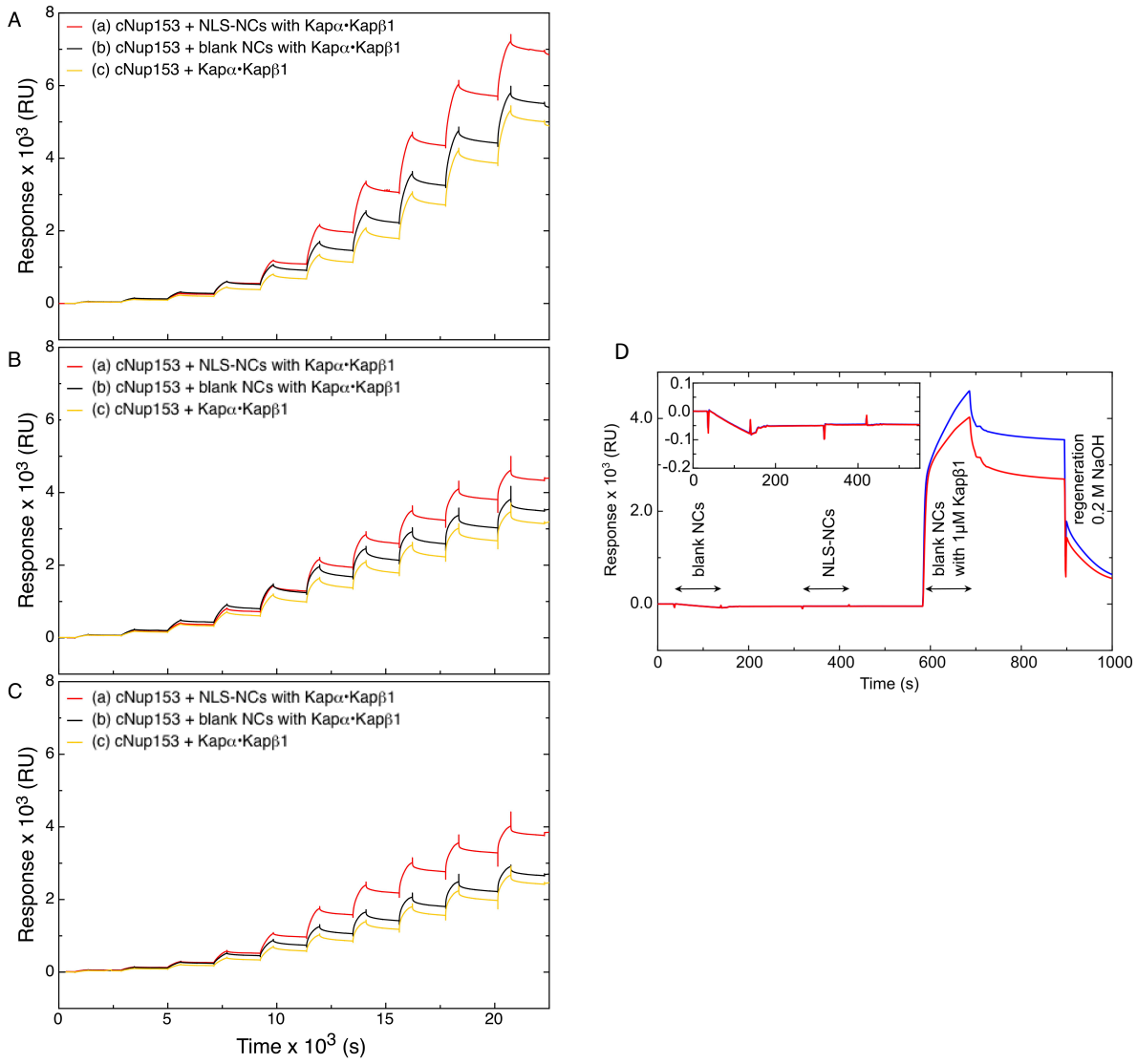

Figure S7. SPR resolves the binding interactions of **(A)** Kapα•Kapβ1-NLS-NCs **(B)** Kapα•Kapβ1 + blank NCs, and **(C)** standalone Kapα•Kapβ1 to cNup153, cNup214 and cNup98, all other conditions being the same. Langmuir isotherm fits are shown in Fig. 4. **(D)** Control SPR measurements demonstrate that NLS-NCs and blank NCs do not interact with Nup98 in the absence of Kapα•Kapβ1. For comparison, Kapβ1 binds efficiently to Nup98. Blue and red lines correspond to measurements obtained in two separate channels.

Table S3: Summary of maximal SPR response signals and equilibrium dissociation constants.

		Nup153	Nup214	Nup98
Kapα•Kapβ1•NLS-NC	R_{max} **(RU)**	8774.7 ± 161	5026 ± 91	4398.6 ± 69
	K_D **(nM)**	18.4 ± 9	8.25 ± 0.5	9.2 ± 0.5
Kapα•Kapβ1 + blank NCs	R_{max} **(RU)**	7036.5 ± 206	3839.4 ± 140	3066 ± 121
	K_D **(nM)**	18.4 ± 1.52	5.17 ± 0.71	8.13 ± 1.14
Kapα•Kapβ1	R_{max} **(RU)**	6888.8 ± 186	3507.8 ± 158	2879.8 ± 137
	K_D **(nM)**	24.8 ± 1.7	5.84 ± 0.97	10.25 ± 1.6

8. Transport assays of blank NCs in permeabilized HeLa cells

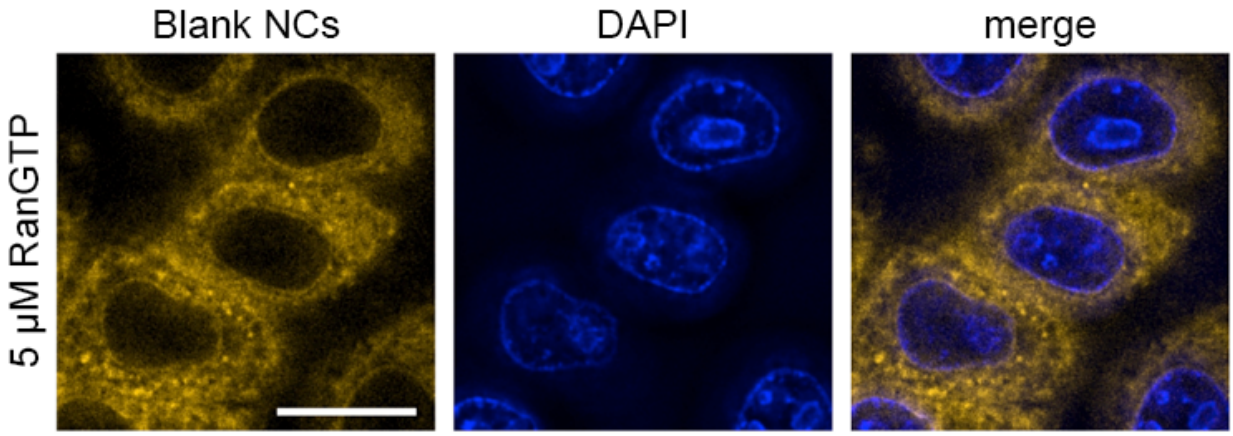

Figure S8. Permeabilized HeLa cells were incubated with 0.6 nM Nile Red-labeled blank NCs in Ran mix. Blank NCs were largely excluded from the nucleus following a 90min incubation time. Scale bar = 10 µm.

9. Nuclear uptake analysis of NLS-NCs and blank NCs in live cells

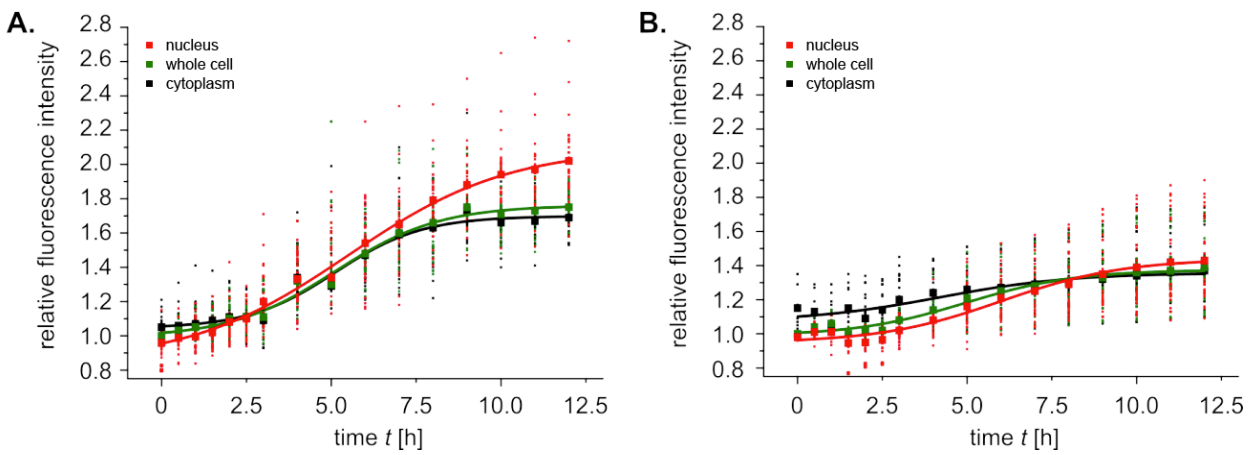

Figure S9. (A) Bodipy-labeled NLS-NCs continue to accumulate in the nucleus but not in the cytoplasm of HeLa cells over a 12 hour period. **(B)** In comparison, Nile Red-labeled blank NCs plateau at similar relative intensities in both compartments within 12 hours.

10. Ultrastructural analysis of NLS-NCs and blank NCs by transmission electron microscopy

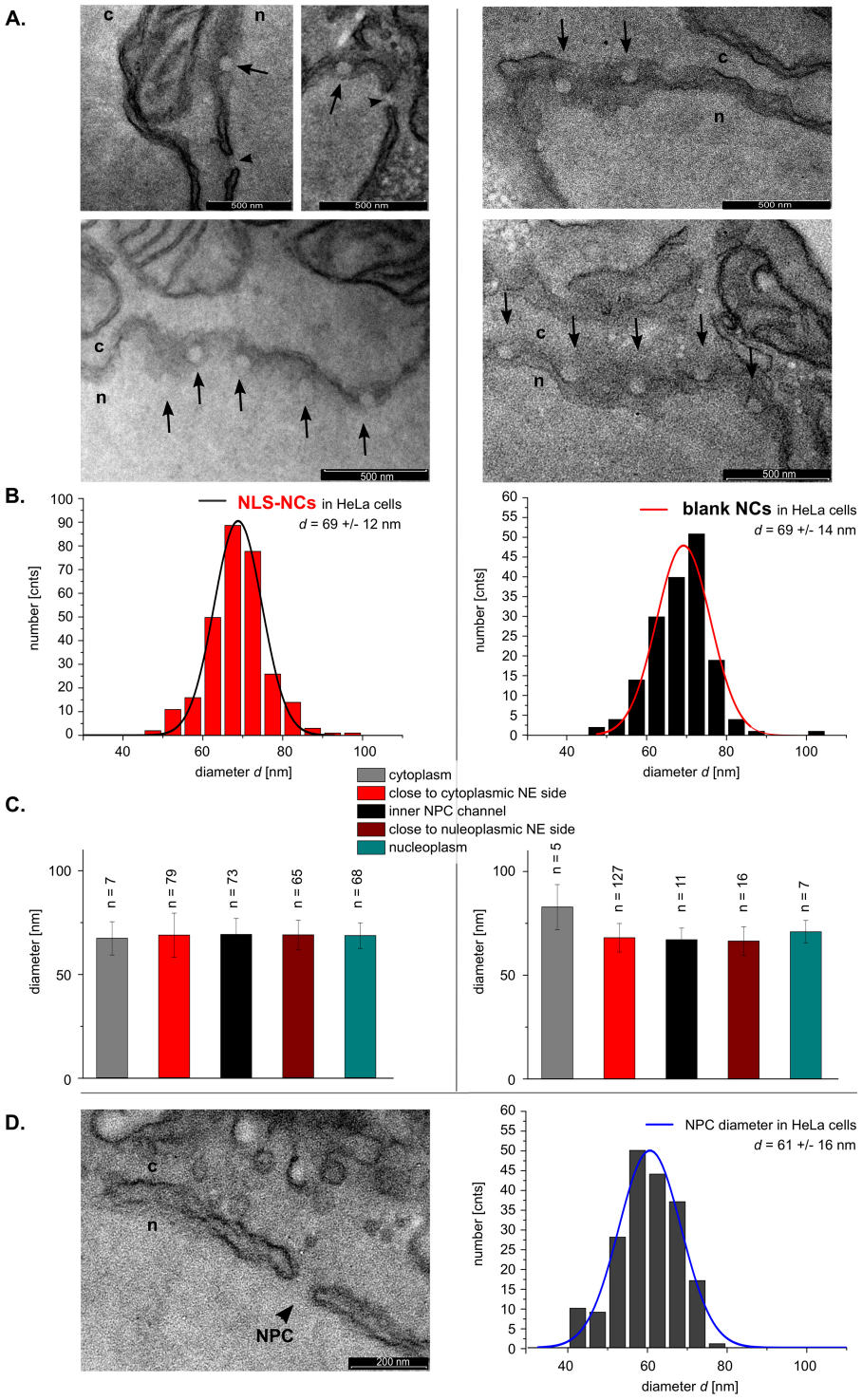

Figure S10. (A) TEM micrographs of HeLa cell sections showing RR-NLS-NCs that have reached the nuclear interior (arrows; left). The nuclear envelope retains RR-blank

NCs in the cytoplasm (arrows; right). **(B)** The average diameter of NLS-NCs and blank NCs are 69 ± 12 nm (n = 292) and 69 ± 14 nm (n = 166), respectively. **(C)** Size distribution of RR-NLS-NCs (left) and RR-blank NCs (right) as a function of location within the cell. **(D)** Statistical analysis of NPC diameter (left) gives an average diameter of 61 ± 16 nm (n = 197; right).

References

1. Nardin C, Hirt T, Leukel J, Meier W (2000) Polymerized ABA triblock copolymer vesicles. *Langmuir* 16:1035-1041.
2. Nardin C, Thoeni S, Widmer J, Winterhalter M, Meier W (2000) Nanoreactors based on (polymerized) ABA-triblock copolymer vesicles. *Chem. Comm.*:1433-1434.
3. Gandini A, Silvestre AJD, Coelho D (2010) Reversible click chemistry at the service of macromolecular materials. 2. Thermoreversible polymers based on the Diels-Alder Reaction of an A-B Furan/Maleimide monomer. *J. Polym. Sci. A* 48:2053-2056.
4. Neubert BJ, Snider BB (2003) Synthesis of (+/-)-phloeodictine A1. *Org. Lett.* 5:765-768.
5. Mantovani G, Lecolley F, Tao L, Haddleton DM, Clerx J, Cornelissen J, Velonia K (2005) Design and synthesis of N-maleimido-functionalized hydrophilic polymers via copper-mediated living radical polymerization: A suitable alternative to PEGylation chemistry. *J. Am. Chem. Soc.* 127:2966-2973.
6. Neises B, Steglich W (1978) 4-Dialkylaminopyridines as acylation catalysts 5. Simple method for esterification of carboxylic-acids. *Angew. Chem. Int. Ed.* 17:522-524.
7. Stauch O, Schubert R, Savin G, Burchard W (2002) Structure of artificial cytoskeleton containing liposomes in aqueous solution studied by static and dynamic light scattering. *Biomacromolecules* 3:565-578.

8. Müller CB, Loman A, Pacheco V, Koberling F, Willbold D, Richtering W, Enderlein J (2008) Precise measurement of diffusion by multi-color dual-focus fluorescence correlation spectroscopy. *EPL* 83:46001.
9. Catimel B, Teh T, Fontes MRM, Jennings IG, Jans DA, Howlett GJ, Nice EC, Kobe B (2001) Biophysical characterization of interactions involving importin-alpha during nuclear import. *J. Biol. Chem.* 276:34189-34198.
10. Bacia K, Schwille P (2007) Practical guidelines for dual-color fluorescence cross-correlation spectroscopy. *Nat. Prot.* 2:2842-2856.
11. Cooper A (2011) *Biophysical chemistry* (The Royal Society of Chemistry, Cambridge, United Kingdom) 2nd Ed.
12. Kruger D, Ebenhan J, Werner S, Bacia K (2017) Measuring Protein Binding to Lipid Vesicles by Fluorescence Cross-Correlation Spectroscopy. *Biophys. J.* 113:1311-1320.
13. Kapinos LE, Schoch RL, Wagner RS, Schleicher KD, Lim RYH (2014) Karyopherin-centric control of nuclear pores based on molecular occupancy and kinetic analysis of multivalent binding with FG nucleoporins. *Biophys. J.* 106:1751-1762.
14. Schoch RL, Kapinos LE, Lim RYH (2012) Nuclear transport receptor binding avidity triggers a self-healing collapse transition in FG-nucleoporin molecular brushes. *Proc. Natl. Acad. Sci. U.S.A* 109:16911-16916.